Applied Materials Today 29 (2022) 101689

Contents lists available at ScienceDirect

Applied Materials Today

journal homepage: www.elsevier.com/locate/apmt

Unexpected enhanced catalytic performance via highly dense interfaces in ultra-fine amorphous-nanocrystalline biphasic structure

Xinjie Peng [a,b], Jiuhui Han [c], Yutian Wang [a,b], Zhenxing Bo [a,b], Anmin Nie [d], Penghui Li [d], Yanying Li [e], Haofei Wu [e], Pan Liu [e], Zhen Lu [a,*], Haiyang Bai [a,f,g,*]

[a] Institute of Physics, Chinese Academy of Sciences, Beijing 100190, China
[b] School of Physical Science, University of Chinese Academy of Sciences, Beijing 100049, China
[c] Frontier Research Institute for Interdisciplinary Sciences (FRIS), Tohoku University, Sendai 980-8578, Japan
[d] Center for High Pressure Science, State Key Laboratory of Metastable Materials Science and Technology, Yanshan University, Qinhuangdao 066004, China
[e] Shanghai Key Laboratory of Advanced High-temperature Materials and Precision Forming, State Key Laboratory of Metal Matrix Composites, School of Materials Science and Engineering, Shanghai Jiao Tong University, Shanghai 200240, China
[f] Center of Materials Science and Optoelectronics Engineering, University of Chinese Academy of Sciences, Beijing 100049, China
[g] Songshan Lake Materials Laboratory, Dongguan, Guangdong 523808, China

ARTICLE INFO

Keywords:
Ultra-fine a/c composite structure
Highly dense interfaces
Degradation efficiency
Amorphous precursor

ABSTRACT

Metallic glasses (MGs) as effective catalysts have been extensively studied due to essentially disordered atomic configurations and widely adjustable micro-morphologies. The catalysis performance could be greatly promoted by introducing additional crystalline phases in the amorphous matrix due to the synergistic advantages of the crystalline and amorphous phases. However, the conventional casting and annealing approaches induced amorphous-crystalline (a/c) composites restrict the synergistic and galvanic cells effects because the generated crystalline phases are easily coarsened with meager a/c interfaces. Here, the artificial ultra-fine a/c $Fe_{76}Si_8B_{13}Nb_3$ catalyst with spinodal decomposition morphology and extremely high dense a/c interfaces of 2×10^{16} m^{-2} are achieved from MG film precursor with nanoscale phase separation by controllable surface diffusion during deposition and suppressive crystalline coarsening procedures. The designed ultra-fine a/c catalyst exhibits admirable cycling degradation property and extraordinary dye degradation efficiency of 300 times than that of the commercial Fe powder. Especially, the outstanding catalytic performances of a/c composite are achieved without the additional involvement of hydrogen peroxide assistance, which provides an environmental-friendly neutral catalytic condition and avoids the corrosive damage during commercial sewage-treatment. This work provides a distinct perspective to design and regulate catalytic performances by amorphous precursor with pre-existent ultra-fine structures.

1. Introduction

Metallic glasses (MGs) with disordered atomic packing arrangement and metastable states [1–4] exhibit distinct mechanical, physical and chemical behaviors such as high strength, strong corrosion resistance, and high surface reactivity [5–10], which are unachievable in their crystalline counterparts. Widely adjustable compositions and atomic structures of MGs provide fascinating possibilities to further improve physical and chemical properties [11–14]. In addition, significant number of low-coordination surface atoms and defect sites promise MGs as precious and competitive newcomers in catalyst fields. For example, NiPdPB, PtCuNiP and IrNiTa MGs exhibit high catalytic activity of hydrogen evolution reaction (HER), oxygen reduction reaction (ORR), and methanol oxidation reaction (MOR) because of the desirable composition, unique morphologies and tunable hierarchical nanostructures [15–17].

MGs catalysts have also been explored for wastewater remediation, in particular, for the degradation of azo dye [18]. Among them, low-cost Fe-based amorphous alloys with distinctive degradation efficiencies exhibit significant potential applications [19]. For example, FeSiBMo amorphous ribbon is firstly applied in azo dye wastewater treatment and presents a higher degradation efficiency than crystalline ribbon [20]; FeSiBNb amorphous powder and FeB amorphous ribbon exhibit outstanding degradation performance than crystalline counterpart or Fe

* Corresponding authors.
E-mail addresses: zhenlu@iphy.ac.cn (Z. Lu), hybai@iphy.ac.cn (H. Bai).

https://doi.org/10.1016/j.apmt.2022.101689
Received 23 June 2022; Received in revised form 24 October 2022; Accepted 7 November 2022

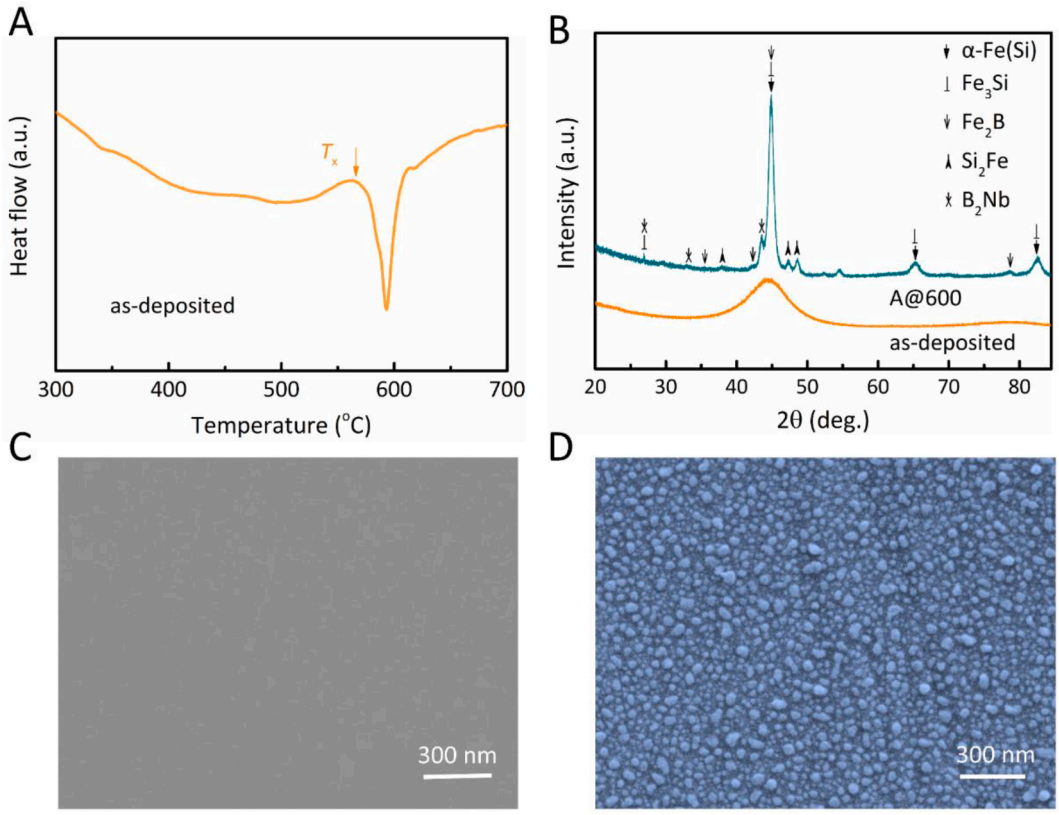

Fig. 1. Thermodynamic, structure and morphologies of Fe-based catalysts. (A) DSC curve of the as-deposited film with obvious glass transition and crystallization signals. (B) XRD profiles of as-deposited and A@600 films. Distinct Bragg peaks confirm the crystallized behavior. (C) and (D) SEM morphologies of as-deposited and A@600 films.

power [21,22]. The enhanced catalytic properties of Fe-based amorphous alloys are usually attributed to the low activation energy for electron transfer, uniform dispersion of active components, and existence of low coordination atoms [23].

Besides, introducing crystal phase from amorphous precursor could further enhance the degradation ability, which is plausibly explained from the perspective of galvanic cells [24–28]. The synergy between grains and amorphous matrix of the amorphous/crystal (a/c) composite structure and the mismatch of the corrosion potential of different phases would make zero-valent iron (Fe^0) to contribute electrons easily and then accelerate the reaction rate [24]. Moreover, the a/c composite with phase boundary and high kinetic energy results in accessorial accessible surface active sites, which could further enhance the charge transfer ability during degradation reaction [29–31]. Nevertheless, composite structures via heterogeneous nucleation by conventional annealing approaches suffer from the limited catalytic efficiency on account of the insufficient number of micro-cells and rare a/c phase boundaries owing to hundreds of nanometers of generated crystals [26–28]. Conventional quenching and annealing procedures with narrow regulation conditions close the door to sufficiently design microstructure and catalysis performances of MGs [19]. In comparison, amorphous films with diverse micro-structures and energy states can be controllably achieved by deposition approach via adjustable deposition parameters and surface diffusion behaviors [32–35].

In this work, FeSiBNb amorphous film with *in-situ* growth of nanoscale spinodal decomposition structure is controllably achieved by rapid surface diffusion through ion-beam deposition (IBD) method, and the bicontinuous a/c dual phase structure with abundant interfaces of 2×10^{16} m^{-2} is constructed by subsequent high-temperature annealing (see section S1). The formation of a/c composite structure improves the catalytic efficiency and cycling performance of MGs, and also provides a new approach for development of catalytic materials via dual amorphous phase precursor with pre-existent nanoscale phase separation.

2. Results and discussion

$Fe_{76}Si_8B_{13}Nb_3$ (atomic ratio) amorphous films were fabricated by IBD method with a constant deposition rate of 3 nm/min with the thickness of 250 nm on flat polymethyl methacrylate (PMMA) substrates. Freestanding film was obtained by immersion into alcohol solution for 10 min (denoted as-deposited film). Fig. 1A displays a typical differential scanning calorimetry (DSC) trace with distinct glassy transition and crystallization signals, which confirm the glassy nature of the freestanding as-deposited film. The subsequent crystallized sample was achieved by fully annealed at 600 °C (above crystallization temperature T_x) for 60 min in a high vacuum environment (below 1.0×10^{-4} Pa) to prevent the possible influence of surface oxidation on the degradation performance. X-ray diffraction (XRD) profile with a broad hump further confirms the amorphous state of the as-deposited film in Fig. 1B. In addition, significant Bragg peaks [α-Fe(Si), Fe_3Si, Fe_2B, $FeSi_2$, B_2Nb] of the annealed film (A@600 film refers to the film annealed at 600 °C) indicate the appearance of obvious crystallization phases after fully annealing [36,37]. Fig. 1C and D present surface morphologies of as-deposited and A@600 films, respectively. Apparently, comparison with the smooth surface of the as-deposited film, dense spherical particles are emerged on the surface of the A@600 film, plausibly inducing by the nucleation of α-Fe(Si) and subsequent grain precipitations and composition aggregations during the long time annealing (Fig. 1D) [27,38].

Fig. 2 presents the degradation behaviors of the Fe-based films in the Direct Blue 6 dye solution (DB 6). Ultraviolet–visible (UV-vis) spectra of extracted reactive solutions at different decolorization time of as-deposited and A@600 films are demonstrated in Fig. 2A and B [39].

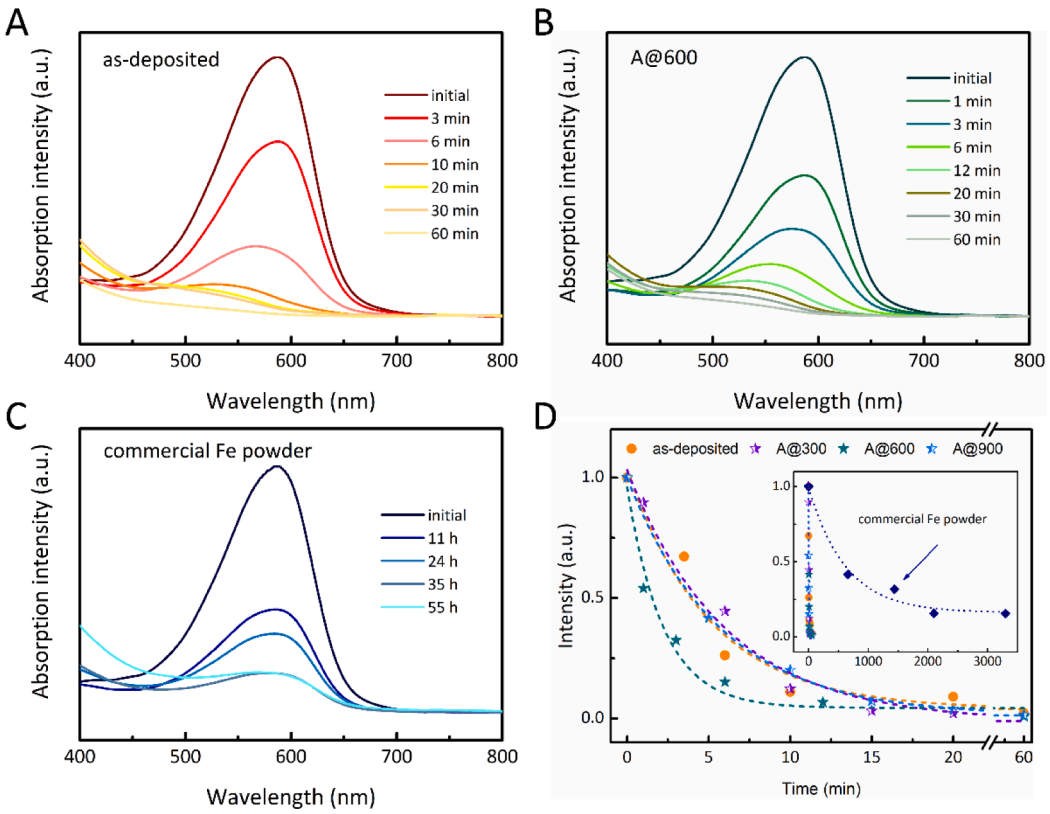

Fig. 2. Catalytic performances of dye degradation catalysts. (A) as-deposited film, (B) A@600 film and (C) pure Fe powders at different time (DB 6 concentration: 40 mg L^{-1}, films and powders dosage: 1 g L^{-1}, temperature: 25 ℃). (D) Normalized absorption intensities around 588 nm as a function of the treatment time for as-deposited, A@300, A@600 and A@900 film. The inset shows the comparison degradation behavior with commercial Fe powder.

As illustrated, the distinct absorbance peak around $\lambda_{max} = 588$ nm arises from the light absorption by DB 6 and the decreasing of peak intensity is attributed from the redox reaction between Fe and azo, in which Fe atoms lose 2 or 3 electrons to form Fe^{2+} or Fe^{3+} ions and the -*N*=*N*- azo bond transforms to -NH_2 by getting 4 electrons [39,40]. The absorption intensity is proportional to the azo dye concentration and gradually decreased with reaction time, indicating the uninterrupted degradation of azo dye [20,41]. As can be seen, the absorption peak of as-deposited and A@600 films are dramatically decreased during the initial 10 min and almost disappeared after 30 min (Fig. 2A and B). In addition, the intensity of absorption peak or the concentration of residual azo solution for the as-deposited film decays more than half within 6 min; while the A@600 film presents much fast reaction rate and exhibits over half degradation within 3 min (Fig. 2A and B). To further clarify the annealing effect on the degradation, the as-deposited film is annealed below the glass transition temperature (T_g) of 300 °C (denoted as A@300 film) and well above the crystallization temperature (T_x) of 900 °C (denoted as A@900 film) for 60 min, respectively. The A@300 film still preserves amorphous structure as shown in section S2 (Fig. S2), while the A@900 film is completely crystallized (Fig. S3). Distinctly, the A@300 film and A@900 film present the slower degradation rate than as-deposited and A@600 films (Table S1). In comparison, the commercial iron powder catalyst needs to take 11 h to achieve the nearly half degradation degree, which is much longer than FeSiBNb films (Fig. 2A–C).

To quantitatively compare the efficiency of four catalysts, the evolutions of absorption intensities with degradation time are plotted in Fig. 2D, together with the commercial Fe powder (inset of Fig. 2D). Obviously, all films present remarkably higher degradation efficiency than commercial iron powder. Degradation rate constant k_{obs} (min^{-1}) is an effective indicator to evaluate the reaction rate, which can be calculated by the first order exponential decay kinetics equation as follows [42]:

$$I_t/I_0 = \exp(-k_{obs}t), \quad (1)$$

where I_t is the normalized intensity of the absorption peak with time, I_0 is a fitting constant, t is the reaction time. The values of k_{obs} are derived to be 0.1960 ± 0.0439 min^{-1}, 0.1653 ± 0.0229 min^{-1}, 0.4525 ± 0.0726 min^{-1}, 0.1748 ± 0.0054 min^{-1} and 0.0016 ± 0.0004 min^{-1} for as-deposited film, A@300 film, A@600 film, A@900 film and the commercial iron powder, respectively. The degradation efficiency of A@600 film exhibits ~2.30 times than that of the as-deposited film and ~300 times faster than that of the commercial iron powder. The excellent decolorization performance of the as-deposited film is attributed to the large number of low-coordination atoms and defects at the surface, which serve as active sites to promote the degradation of azo dye [23]. The subsequence thermal annealing below T_g assists the diffusion of surface low-coordination atoms towards the thermodynamic stabilization state and thus reduces the degradation efficiency of A@300 film [43]. Annealing above T_x will dramatically consume the free volumes and achieve an equilibrium state, which is supposed to depress the degradation efficiency. Therefore, the degradation efficiency of fully crystalline A@900 film is lower than that of as-deposited film. Whereas the A@600 sample with distinct crystal phases exhibits the highest degradation efficiency, suggesting a different reaction acceleration mechanism in comparison to as-deposited, A@300 and A@900 samples.

Fig. 3A presents the high-resolution transmission electron microscopy (HRTEM) image of the as-deposited film. Clear heterogeneous amorphous phases with average sizes of ~1.4 ± 0.5 nm and ~4.7 ± 1.5 nm (inset of Fig. 3A) indicate a pre-existing nanoscale phase separation during deposition. Corresponding selected area electron diffraction (SAED) with obvious split diffraction halo rings further confirms the phase separation with two different average local atomic configuration environments of the as-deposited film (Fig. 3B). Mass-sensitive scanning

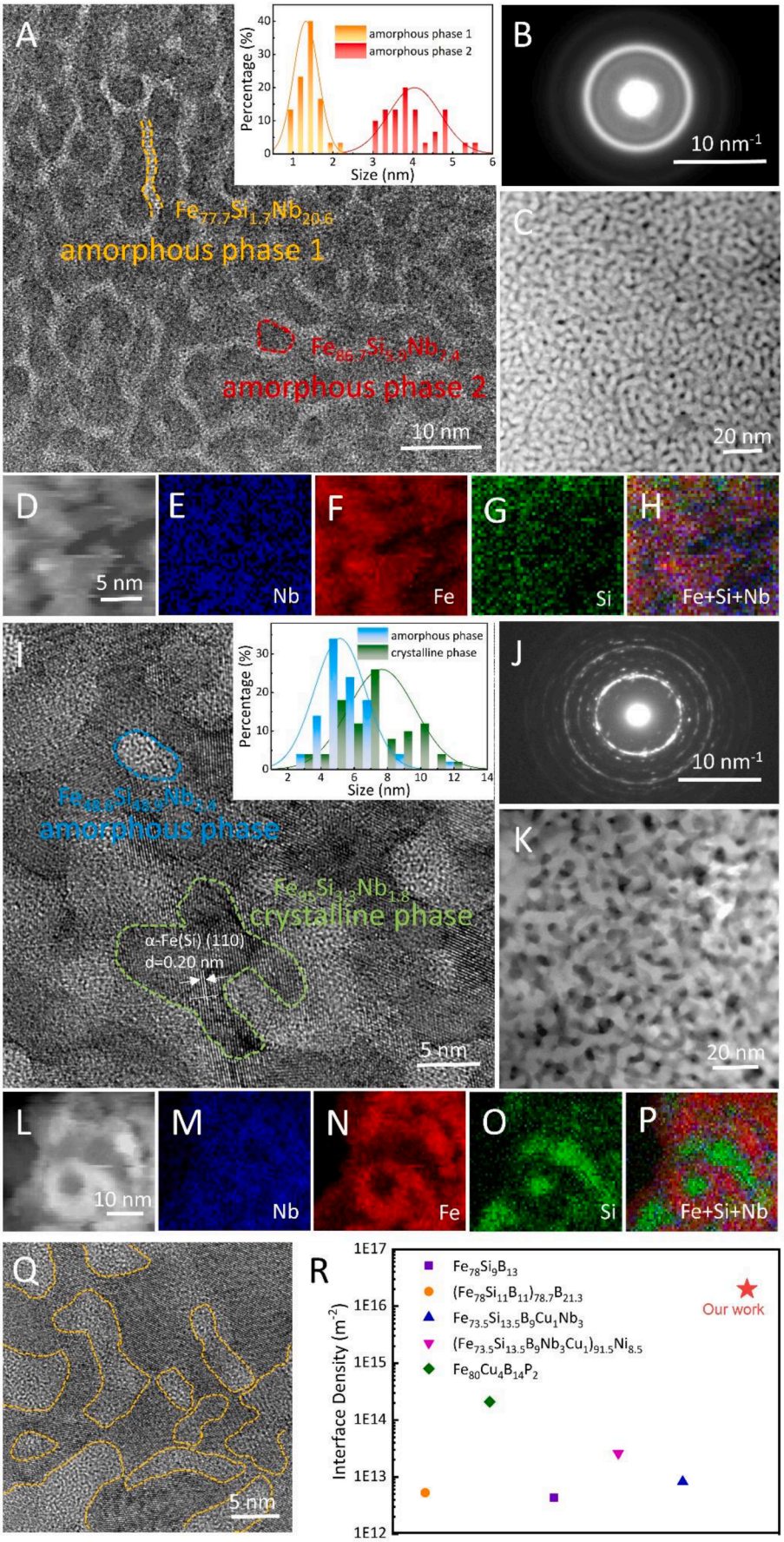

Fig. 3. Microstructure characterization of as-deposited and A@600 films. (A) HRTEM image of the as-deposited film. The inset shows the size distribution of two amorphous phases. (B) SAED patterns of the as-deposited film. (C) STEM image of the as-deposited film. (D–H) EDS mappings of Nb, Fe and Si of as-deposited film, EDS mappings are normalized by the maximum pixel intensity, respective. (I) HRTEM image of A@600 film. The inset shows the size distribution of amorphous phase and crystalline phase. Method for marking crystal plane spacing is shown in the Summplementary Material of Section S3. (J) SAED patterns of A@600 film. (K) STEM image of A@600 film. (L-P) EDS mappings of Nb, Fe and Si of A@600 film. (Q) HRTEM image of A@600 film with a/c structure. Dotted yellow lines delineate boundaries between the amorphous and crystalline phases. (R) The interface densities of $Fe_{78}Si_9B_{13}$ [27], $(Fe_{78}Si_{11}B_{11})_{78.7}B_{21.3}$ [62], $Fe_{73.5}Si_{13.5}B_9Cu_1Nb_3$ [27], $(Fe_{73.5}Si_{13.5}B_9Nb_3Cu_1)_{91.5}Ni_{8.5}$ [26] and $Fe_{80}Cu_4B_{14}P_2$ [28] with a/c structures.

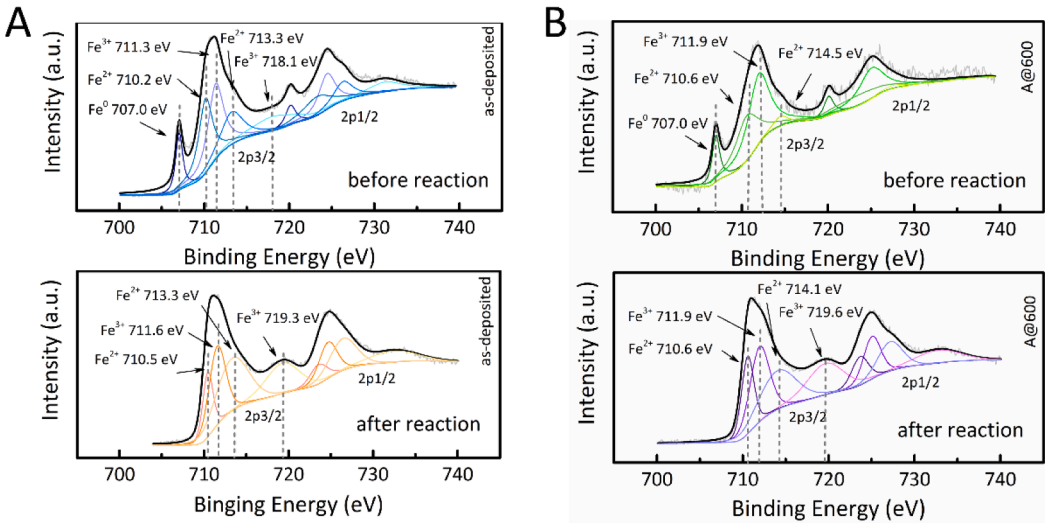

Fig. 4. Surface elemental analysis. (A) XPS fitting curves of Fe 2p for as-deposited film before and after degradation reaction. (B) XPS fitting curves of Fe 2p for A@600 film before and after degradation reaction.

transmission electron microscopy (STEM) with a high-angle annular dark-field (HAADF) detector was utilized to further uncover the structural signatures. As shown in Fig. 3C, the HAADF-STEM image of the as-deposited film exhibits an analogous spinodal decomposition morphology with the average sizes of ~1.6 ± 0.4 nm and ~4.2 ± 0.6 nm, which is consistent with the HRTEM results and undoubtedly indicates the nanoscale spatial heterogeneity in the as-deposited film [44]. In addition, TEM image of the cross-section presents uniform distributed of spinodal decomposition morphology along the growth direction, suggesting a well distributed three-dimensional nanoscale phase separation structure in the as-deposited film (Fig. S5). Energy dispersive spectroscopy (EDS) mappings with a spatial resolution of 3 Å were applied to reveal the detailed elemental distributions. The aggregation of Fe is clearly presented in Fig. 3F and Nb is concentrated at the interface of two amorphous phases according to the merged elemental mapping (Fig. 3H), whereas Si is nearly homogeneous distributed in both glassy phases. Accordingly, the HRTEM and HAADF-STEM images of the A@600 film also exhibit distinct phase separation with similar morphology of as-deposited sample (Fig. 3I and K). Besides, obvious nanocrystalline phase is formed with an average size of ~7.7 ± 1.9 nm as shown in Fig. 3I and K. Nevertheless, a portion of glassy phase is still maintained even after high temperature and long-time annealing (Fig. 3I and K), demonstrating the high resistance to crystallization of the dual phase glassy film, and thus constructing an a/c composite structure (Fig. 3I and K). Remarkably, characteristic width of two phases is slightly increased by several nanometers after annealing above the corresponding T_x, which is opposite with previous reports and suggests a restricted nucleation and subsequent growth mechanism [26–28]. The pre-existence of ultra-fine nanoscale spinodal decomposition morphology and the depressed crystal growth generate an extreme dense of a/c interfaces of 2×10^{16} m^{-2} (Fig. 3Q, see section S1 for details), which is greatly higher than typical nanocrystal interfaces induced by conventional annealing method via glassy precursor (Fig. 3R). Fig. 3L–P present EDS mappings of the A@600 film. Dark regions in Fig. 3L are identified as amorphous phase with the aggregation of Si and B (Figs. 3O and S6), and white regions are composed by Fe-rich nanocrystal phase (Fig. 3N). Furthermore, Nb is still concentrated at the interface of the amorphous and nanocrystal phases as shown in Fig. 3M and P. It is suggested that the formation of nanocrystals during heat treatment can be attributed to the exhaustion of Si and B, and aggregation of Fe from amorphous precursors through the Nb concentrated interfaces via bulk diffusion, which could depress the coarsening of nanocrystals at elevated temperature [45–47].

Because FeSiBNb presents negative enthalpy of mixing values for all atomic pairs (Table S2) [48], the phase separation should be prohibitive from the thermodynamics perspective. However, large differences of mixing enthalpy between atom pairs are expected to increase the tendency for formation of element segregation, which could result in nano-scale phase separation [44]. Fast deposition rate benefits the composition aggregation during the sedimentary process, which is driven by the kinetic energy of surface deposited atoms [49]. With the decrease of deposition rate, sufficient surface diffusion drives the glass toward homogeneous structure with thermodynamically favored state as shown in Fig. S7. The microstructure evolution observed by TEM indicates that the nanoscale phase separation is initially formed by the surface diffusion through IBD method, and the followed a/c composite structure via annealing introduces abundant a/c phase boundaries. The a/c composite structure combines the two advantages of the high conductivity of the crystalline phase (promoting electron transfer) and abundant unsaturated coordination sites in amorphous phase and a/c phase boundaries (providing plentiful active sites) [31]. In addition, a/c phase boundaries can modulate the electron densities of the interfacial sites and promote the charge-transfer process [31]. The divergent ultra-fine nanoscale composite structure thus has a positive impact on catalytic behavior [29].

Since the degradation of azo dye is a surface-controlled mechanism, X-ray photoelectron spectroscopy (XPS) is utilized to analyze the chemical environment of surface elements (full spectrum shown in Fig. S8). Actually, the valence state of surface oxide layers is rather complex, but several phenomena could be still revealed. Due to the main role of Fe in the degradation process, the chemical state of Fe before and after the degradation reaction is mainly analyzed as show below. It can be found in Fig. 4 that a mixture of Fe^0 (707.0 eV), FeO_x (Fe^{2+}, 710.2/713.3, 710.6/714.5 eV), Fe_2O_3 and FeOOH (Fe^{3+}, 711.3/718.1, 711.9 eV) co-exists on the surface layer of as-deposited and A@600 films before reaction with relative proportions of Fe^0, Fe^{2+} and Fe^{3+} as 10.14%, 45.43%, 44.43% and 11.8%, 49.46%, 38.74%, respectively [50]. For the films after reaction, the surface layer consists of FeO_x (Fe^{2+}, 710.5/713.3, 710.6/714.1 eV), and Fe_2O_3 and FeOOH (Fe^{3+}, 711.6/719.3, 711.9/719.6 eV) [51–53], relative proportions are shown in Table S3. In addition, obvious Fe-O/FeOOH (Fe^{3+}, 711.9 eV) and Si-O (Si^{4+}, 102.8 eV) peaks demonstrate that a thin oxidation layer is formed on the A@600 film surface on account of the subsequent heat treatment of the as-deposited film. The surface oxidation thin layer assists the adsorption of azo dye on the surface and acts as a mediator in the electron transfer reaction [54]. Besides, the Fe 2p peak of the A@600

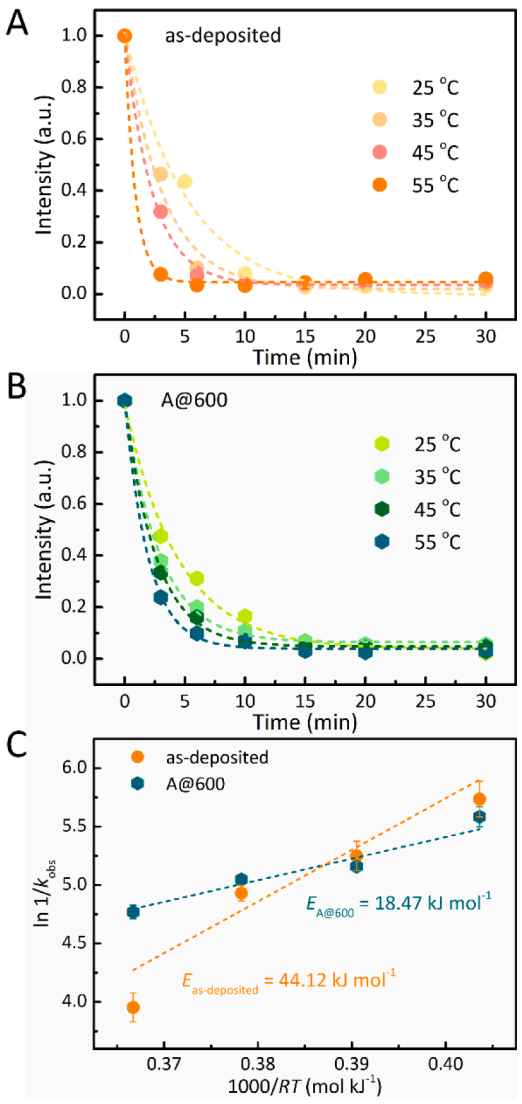

Fig. 5. The evaluation of degradation behaviors with different reaction temperatures. The normalized UV absorption intensities versus the reaction time at different temperatures for (A) as-deposited film and (B) A@600 film (DB 6 concentration: 40 mg L^{-1}, films and powders dosage: 0.83 g L^{-1}, temperature: 25, 35, 45 and 55 ℃). The dotted curves are exponential fitted to data points. (C) The Arrhenius plots of ln1/k_{obs} versus 1000/RT for (A) as-deposited and (B) A@600 films.

film exhibits higher binding energy than the as-deposited film, indicating that Fe sites in the A@600 film have stronger electronic interactions with metalloid elements [55,56]. The distinct chemical environment and favorable adsorption of dye molecular at the surface are reasonable for the improved catalytic performance for dye degradation.

Fig. 5A and B exhibit the normalized degradation rate of as-deposited and A@600 films with a series of reactive temperatures. Both catalysts exhibit accelerated reaction behaviors at elevated temperatures during the first 10 min and unanimously approach zero after 15 min for different degradation temperatures. Moreover, the degradation rate of A@600 film is much faster than the as-deposited one for all temperatures. Determination of reaction rates (k_{obs}) under different temperatures provides insights on the reaction mechanisms, which can be well described by the following Arrhenius equation:

$$\ln(k_{obs}) = -E_a/RT + \ln(A), \quad (2)$$

where E_a is the degradation activation energy, R is the gas constant, A is a pre-exponential factor. A good linear relationship between ln(k_{obs}) and $1/T$ can be obtained for both catalyst films, verifying that the chemical degradation reaction is a thermal activation-controlled process (Fig. 5C). The activation energy E_a for the as-deposited and A@600 films are determined to be 44.12 ± 12.36 kJ mol^{-1} and 18.47 ± 4.03 kJ mol^{-1}, respectively. Remarkably, the activation energy of A@600 film falls in the mass transport limited process with the activation energy of 8–21 kJ mol^{-1} [57], and the as-deposited film with higher activation energy suggests a surface reaction controlled degradation reaction process (>29 kJ mol^{-1}) [58,59]. The mass transport limited mechanism demonstrates that the degradation reaction barrier for the A@600 film is low, and the rate is controlled by the transportation of reactant in the solution.

In order to demonstrate the reusability of catalysts, azo dye degradation cycling test of as-deposited and A@600 films is carried out with reaction time of 30 min for each cycling, and the cycling reaction time of pure Fe powders is 48 h for comparison (Fig. 6A–C). Fig. 6D shows the corresponding reaction rate of three samples. The degradation efficiency of as-deposited film gradually decreases in the first three cycles (>80%), and only presents ~50% degradation efficiency after fourth cycles (Fig. 6A). However, the A@600 film still keeps high degradation capability after fourth cycles with the degradation efficiency near 100% and exhibits perceptible declined degradation efficiency after fifth cycles (~80%) as shown in Fig. 6B. Besides, the A@600 film presents enhanced degradation efficiency and reaction rate of the second cycling (Fig. 6B and D), which suggests a rejuvenated catalytic performance of A@600 film [27]. As for pure Fe powders, under the premise of ultrasonic cleaning after each reaction (the heavily oxidized Fe powder cannot even complete the second repeated test without ultrasound cleaning), the reusability can be barely compared with amorphous films under an extremely long reaction time (Fig. 6C).

Because the degradation of azo dyes is a surface-mediated process [60], the surface morphologies of the films after reaction are depicted in Fig. 7. Flocculent-like substances are clearly adhered on the surface of both films (Fig. S9A), which are reacted sediments from DB 6 degradation process and can be easily removed by ultrasonic cleaning. Representative network structures are formed at the surface of as-deposited and A@600 films (Fig. 7A and C), which is interwoven by reaction products at the top layer and exposed a fresh inside iron matrix skeleton (Fig. 7B). Combined with elemental mappings in Fig. 7E, it is inferred that the light-colored interweave on the top layer is metal oxidation produces (the concentration of O is shown in Fig. S10A). The degree of degradation can be reflected from the furrowed surface morphology after reaction (Fig. S9B), the more electrons the film provides, the more light-colored reaction products the surface interweaves. The unique skeleton structure increases the surface active site and also provides a channel for the mass and electron transmission, which is conducive to the further degradation [28]. In addition, the formation of network structure by microalloying of non-metallic elements Si and B hinders the generation of dense metal oxide film at the surface, and thus ensures a continuous degradation process [28]. The A@600 film presents diversified morphologies as shown in Figs. 7C, D and S9C–F. Except for the network structure, dark areas with irregularly shape are randomly distributed at the surface of film (Figs. 7C, D and S9B–F). Combined with elemental mappings in Fig. 7F, it can be clearly observed that the heterogeneous regions of each element, especially the Fe element, have low content in the dark regions (Fig. S10B and C), indicating that the concentrated electron exchange takes place and exhausts Fe as fast reaction sites and thus presents faster degradation rate than as-deposited film [24].

Compared with as-deposited film and Fe powder, the A@600 film exhibits the best reusable performance. Ubiquitous corrosion pits with dark contrast coexists with network structures on the surface of the A@600 film as shown in Fig. 7C. These corrosion pits are plausibly originated from the uneven surface of the A@600 film with aggregation of α-Fe(Si) spherical particles, which could consume Fe intensively and

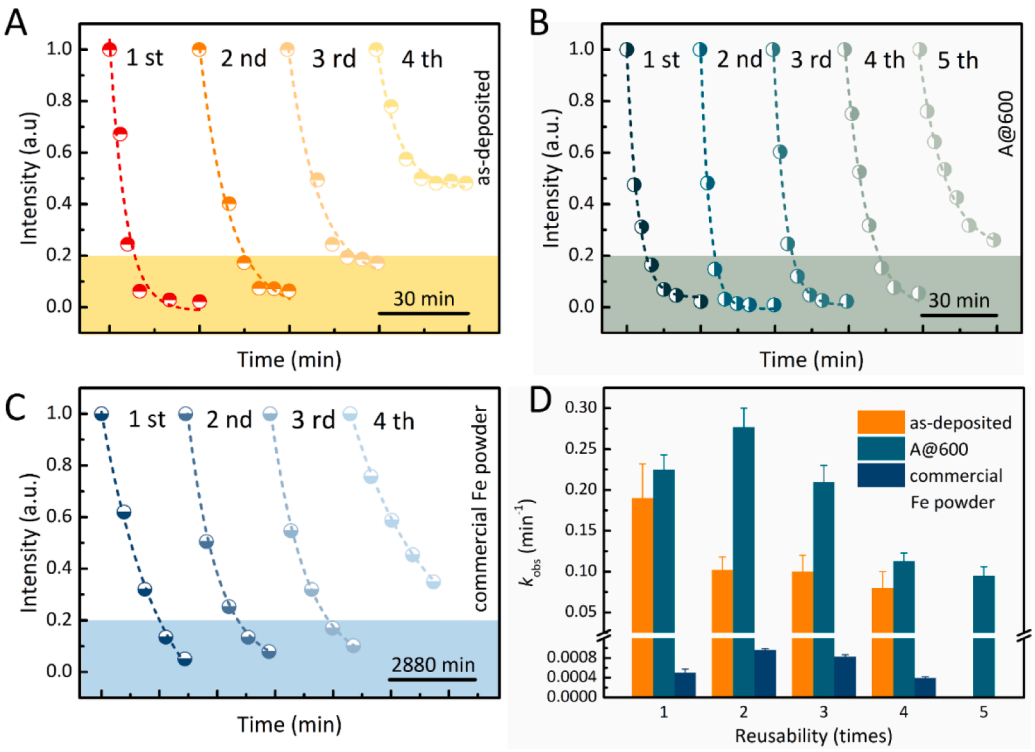

Fig. 6. Cycling degradation performance of dye degradation catalysts. (A-C) The cycling degradation performance of as-deposited film, A@600 film and pure Fe powders, respectively (DB 6 concentration: 40 mg L^{-1}, films and powders dosage: 0.83 g L^{-1}, temperature: 25 ℃). (D) The degradation rate k_{obs} at different cycling tests for as-deposited film, A@600 film and commercial Fe powder.

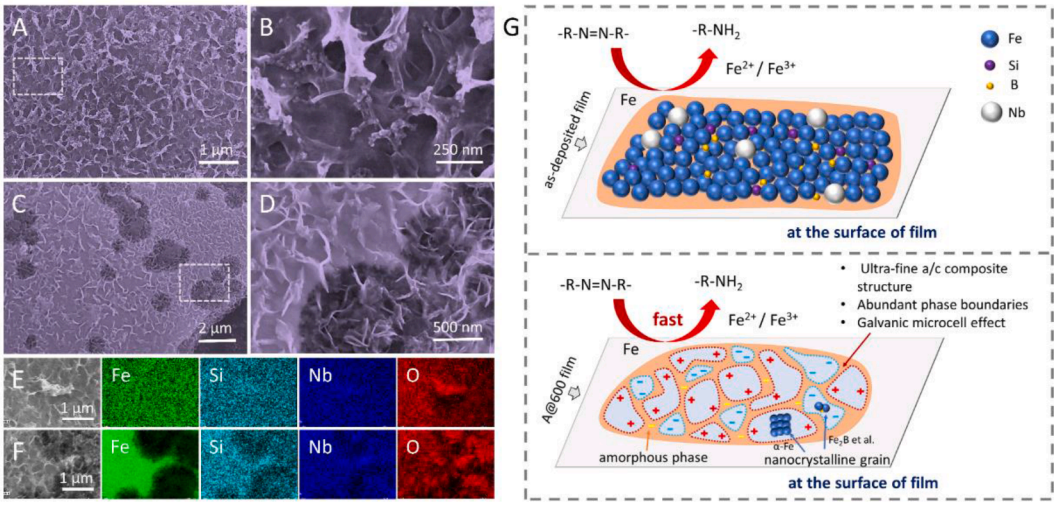

Fig. 7. Surface morphology of $Fe_{76}Si_8B_{13}Nb_3$ films after reaction. (A,B) as-deposited film. (C,D) A@600 film. (E) and (F) Elemental mappings of Fe, Si, Nb and O for as-deposited and A@600 films, respectively. The EDS mapping of each element is normalized by maximum pixel intensity to reveal the relative spatial distribution of each element. (G) Schematic of catalytic degradation process for as-deposited and A@600 films. The orange regions represent the amorphous phase (the two amorphous phases are not distinguished in top panel) and the blue regions represent the crystalline phases (bottom panel). There are potential differences between nanocrystalline and amorphous phases, as well as α-Fe(Si) phase (surrounded by red dotted line) and other intermetallics (surrounded by blue dotted line).

thoroughly during reaction (Figs. 7F and S10C). While other regions with less Fe consumption can become the electron reservoir for the further reaction, reflected in EDS element distribution mappings of Fe and O (Figs. 7E, F and S10 for comparison). Moreover, the network architectures can provide paths for the diffusion of dye molecules to react with fresh exposed α-Fe (Si) nanocrystals, which leads to higher reaction rate in the second cycle of A@600 film (Fig. 6D). After 4th or 5th cycles, all of Fe-based catalysts exhibit rapidly depression of degradation efficiency (Fig. 6), which can be attributed to the severe surface oxidation and intrinsic mass loss after multiple reactions (Figs. S11 and S12).

It is reasonable to believe that the differences of degradation rate and reutilization property between as-deposited and A@600 films are related to their discrepancy phase structures [24–28]. Fig. 7G presents a schematic illustration of degradation process. Additional free volumes in as-deposited film could be acted as "active site" and permit high reaction activity [21], and intrinsic hyperfine bicontinuous phase separation structure could form plentiful galvanic microcells via the potential

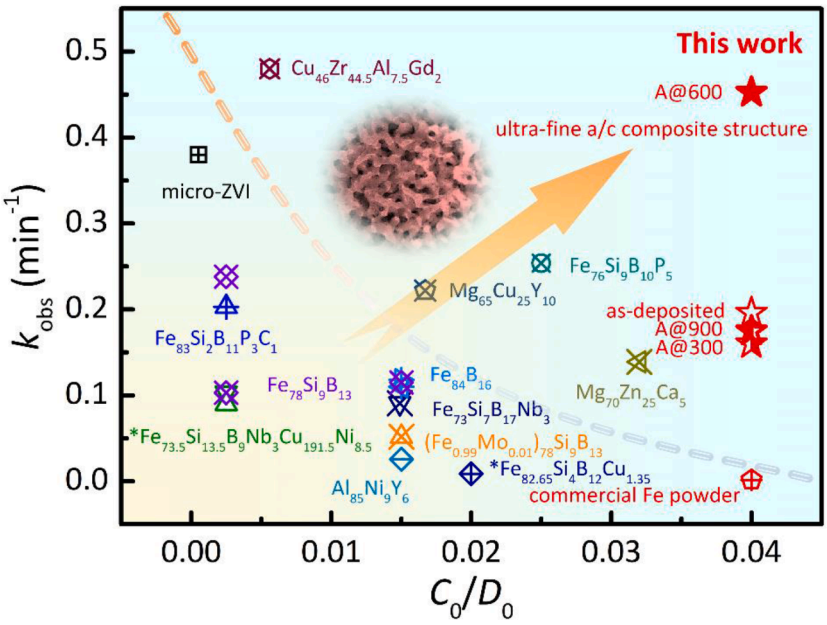

Fig. 8. Comparison of dye degradation performance (Fenton-like reactions are not included). Degradation rate versus dosage ratio for different metallic glasses and crystalline ZVI catalysts. The asterisk represents nanocrystalline material and our catalyst is marked by red pentagram. More details are summarized in Table S4 of section S7.

differences of two phases in the degradation process of azo aqueous solution, thus exhibiting outstanding degradation rate than commercial Fe powder. The annealed A@300 film with less free volumes results a depressed degradation property, and complete crystallized A@900 film exhausts all free volumes and generates the worst degradation efficiency (Table S1). However, the annealed A@600 film presents the highest degradation performance, suggesting a different stimulative catalytic mechanism. In comparison with as-deposited and A@900 films, the A@600 film has an ultra-fine a/c composite structure after annealing, which could further strengthen the galvanic microcell effect on account of the distinct compositions between amorphous and crystal phases. In addition, the crystal counterpart with low electrical resistivity facilitates the transportation of electrons. Furthermore, a/c phase boundaries with high dense of vacancies could act as "active site" and also modulate the electronic structure of the interfacial sites during catalytic process [31]. In consequence, the A@600 film presents the remarkable catalytic performance with the low activation energy.

To further compare the degradation behaviors, the relationship between the degradation rate k_{obs} and the ratio of dye concentration to catalyst mass concentration C_0/D_0 [initial dye concentration C_0 (g L^{-1}), catalyst dosage D_0 (g L^{-1})] for the Fe-based amorphous alloys and crystalline zero valent iron (ZVI) is well plotted in Fig. 8, more details are listed in Table S4. Obviously, the A@600 film with nanoscale ultra-fine a/c composite structure presents both high reaction rate and low consumption of catalyst dosage marked in Fig. 8.

3. Conclusion

In summary, the A@600 $Fe_{76}Si_8B_{13}Nb_3$ film with ultra-fine dual phases presents about 300 times dye degradation efficiency than that of commercial Fe powder catalyst. The high degradation efficiency of A@600 film can be attributed to the synergistic effect of nanocrystals and amorphous matrix, which promotes the formation of galvanic cells, accelerates electron transport by low electrical resistivity and improves intrinsically enhanced activity sites from abundant phase boundaries. The generated low activation energy demonstrates a mass transport limited degradation mechanism. Furthermore, enduring cycle performance of the A@600 film with H_2O_2 free and maintenance free degradation environment benefits the commercial applications for wastewater disposal. This work demonstrates the potential of metallic glasses with adjustable structure for catalytic applications, and more importantly, provides a new approach to design and develop ultra-fine a/c composite catalytic material via nanoscale phase separation precursor.

4. Materials and methods

4.1. Materials preparation

$Fe_{76}Si_8B_{13}Nb_3$ amorphous films were fabricated by ion beam assisted deposition (IBAD) on a flat polymethyl methacrylate (PMMA) plate. The base pressure before deposition was better than 4.0×10^{-4} Pa, and the deposition environmental pressure was maintained at 2.6×10^{-2} Pa by high purity argon supplement. The ion beam with energy of 750 eV bombards the target, and the sputtered atoms are deposited on the substrate with a thickness of 250 nm. The film was immersed in alcohol for 10 min to peel from the PMMA substrate (alcohol reduces the van der Waals force between the film and the substrate) [61]. As-deposited films were annealed at 300, 600 and 900 °C for 1 h in a high vacuum tube furnace with the base pressure better than 1.0×10^{-4} Pa. As-deposited (fully amorphous), A@300 (amorphous), A@600 (amorphous-nanocrystalline composite), and A@900 (fully crystalline) $Fe_{73}Si_7B_{17}Nb_3$ films were treated with ultrasonic for 5 min in alcohol with a fragmentary size of ~50 μm. The final transmission electron microscopy specimens were prepared by ion milling (Gatan, PIPS II 695) with 3 kV and finally polished with low-voltage (0.5 kV) with a liquid-nitrogen-cooled stage.

4.2. Catalytic properties

The azo dye (Direct Blue 6, $C_{32}H_{20}N_6Na_4O_{14}S_4$) was purchased from Sinopharm Chemical Reagent Co. Ltd. Direct Blue 6 powder was dissolved in deionized water with the concentration of 40 mg L^{-1}. The film fragments of 30 mg were added into 30 mL solution for each time. Zero-valent Fe (Fe^0) powder with 300 mesh was used for comparation. The dye solution with film fragments were conducted in a thermostatic water bath to obtain the constant temperatures (i.e., 25, 35, 45, and 55 °C). The absorption spectra of reacted solution were characterized by a dual-beam ultraviolet visible spectrophotometer (TU-1901) in the

wavelength range of 400–800 nm. For cycling experiments, Fe powders were washed by ultrasonic in alcohol for 3 min.

4.3. Characterization

The structures of as-deposited, A@300, A@600 and A@900 films were examined by X-ray diffractometry (XRD) with Cu-K_α radiation (Bruker D8 Advance). The high-resolution transmission electron microscopy (HRTEM) images, selected area electron diffraction (SAED) patterns and energy-dispersive X-ray spectroscopy (EDS) mappings of sample were characterized by a JEM-2100F TEM (JEOL, 200 kV) equipped with double spherical aberration (Cs) correctors for both the probe-forming and image-forming lenses. The EELS elemental mapping was simultaneously recorded with the Gatan GIF Quantum system on STEM mode by a transmission electron microscope (JEOL ARM 200F) equipped with a cold emission gun and an aberration corrector for the probe-forming lens system. The surface morphologies were investigated by scanning electron microscopy (SEM, SU5000, 15 kV). The surface elemental analysis was determined by X-ray photoelectron spectroscopy (XPS) using a ThermoFisher Scientific spectrometer (ESCALAB 250X) with an Al K_α radiation source.

Data and materials availability

The data that support the findings of this study are available from the corresponding author upon reasonable request.

CRediT authorship contribution statement

Xinjie Peng: Methodology, Investigation, Validation, Writing – original draft. **Jiuhui Han:** Resources, Data curation. **Yutian Wang:** Resources, Data curation. **Zhenxing Bo:** Resources, Data curation. **Anmin Nie:** Resources, Data curation. **Penghui Li:** Resources, Data curation. **Yanying Li:** Resources, Data curation. **Haofei Wu:** Resources, Data curation. **Pan Liu:** Resources, Data curation. **Zhen Lu:** Conceptualization, Writing – review & editing, Supervision, Project administration, Funding acquisition. **Haiyang Bai:** Conceptualization, Writing – review & editing, Supervision, Project administration, Funding acquisition.

Declaration of Competing Interest

The authors declare that they have no known competing financial interests or personal relationships that could have appeared to influence the work reported in this paper.

Data availability

Data will be made available on request.

Acknowledgments

This work was supported by the National Key R&D Program of China (Grant No. 2021YFB3802900), the Major Program of National Natural Science Foundation of China (Grant No.52192600, 952192601), the Hundred Talents Program of Chinese Academy of Sciences. This work is supported by the Center for Materials Genome.

Supplementary materials

Supplementary material associated with this article can be found, in the online version, at doi:10.1016/j.apmt.2022.101689.

Appendix A. Supplementary data

The following are the Supplementary data to this article.

References

[1] A.L. Greer, Metallic glasses, Science 267 (31) (1995) 1947.
[2] W.L. Johnson, Bulk glass-forming metallic alloys: Science and technology, MRS Bull. 24 (10) (1999) 42.
[3] A. Inoue, Stabilization of metallic supercooled liquid and bulk amorphous alloys, Acta Mater. 48 (1) (2000) 279.
[4] P.G. Debenedetti, F.H. Stillinger, Supercooled liquids and the glass transition, Nature 410 (8) (2001) 259.
[5] A. Baiker, Metallic glasses in heterogeneous catalysis, Faraday Discuss. Chem. Soc. 87 (1989) 239.
[6] A.L. Greer, E. Ma, Bulk metallic glasses: at the cutting edge of metals research, MRS Bull. 32 (8) (2011) 611.
[7] Y.Q. Cheng, E. Ma, Atomic-level structure and structure–property relationship in metallic glasses, Prog. Mater. Sci. 56 (4) (2011) 379.
[8] J. Schroers, Bulk Metallic Glasses, Phys. Today 66 (2) (2013) 32.
[9] E. Ma, Tuning order in disorder, Nat. Mater. 14 (6) (2015) 547.
[10] Y.H. Sun, et al., Thermomechanical processing of metallic glasses: extending the range of the glassy state, Nat. Rev. Mater. 1 (9) (2016) 16039.
[11] B. Zberg, et al., MgZnCa glasses without clinically observable hydrogen evolution for biodegradable implants, Nat. Mater. 8 (11) (2009) 887.
[12] S. Mukherjee, et al., Palladium nanostructures from multi-component metallic glass, Electrochim. Acta 74 (2012) 145.
[13] A. Inoue, A. Takeuchi, Recent development and application products of bulk glassy alloys, Acta Mater. 59 (6) (2011) 2243.
[14] M. Carmo, et al., Bulk metallic glass nanowire architecture for electrochemical applications, ACS Nano 5 (4) (2011) 2979.
[15] S. Mukherjee, et al., Tunable hierarchical metallic-glass nanostructures, Adv. Funct. Mater. 23 (21) (2013) 2708.
[16] G. Doubek, et al., Guided evolution of bulk metallic glass nanostructures: A platform for designing 3D electrocatalytic surfaces, Adv. Mater. 28 (10) (2016) 1940.
[17] Z.J. Wang, et al., Low-iridium-content IrNiTa metallic glass films as intrinsically active catalysts for hydrogen evolution reaction, Adv. Mater. 32 (4) (2020), e1906384.
[18] M.M. Khan, et al., Recent advancements in bulk metallic glasses and their applications: a review, Crit. Rev. Solid State 43 (3) (2017) 233.
[19] L.C. Zhang, S.X. Liang, Fe-based metallic glasses in functional catalytic applications, Chem. Asian J. 13 (23) (2018) 3575.
[20] C.Q. Zhang, et al., Decolorization of azo dye solution by Fe-Mo-Si-B amorphous alloy, J. Non Cryst. Solids 356 (33–34) (2010) 1703.
[21] J.Q. Wang, et al., Rapid degradation of azo dye by Fe-based netallic glass powder, Adv. Funct. Mater. 22 (12) (2012) 2567.
[22] Y. Tang, et al., Rapid decomposition of Direct Blue 6 in neutral solution by Fe-B amorphous alloys, RSC Adv. 5 (8) (2015) 6215.
[23] S. Das, et al., Bi-functional mechanism in degradation of toxic water pollutants by catalytic amorphous metals, Adv. Eng. Mater. 18 (2) (2016) 214.
[24] P.P. Wang, et al., Fast degradation of azo dye by nanocrystallized Fe-based alloys, Sci. China Phys. Mech. 60 (7) (2017), 076112.
[25] S. Chen, et al., Multi-phase nanocrystallization induced fast degradation of methyl orange by annealing Fe-based amorphous ribbons, Intermetallics 90 (2017) 30, 2017.
[26] S. Chen, et al., Unexpected high performance of Fe-based nanocrystallized ribbons for azo dye decomposition, J. Mater. Chem. A 5 (27) (2017) 14230.
[27] S.X. Liang, et al., Compelling rejuvenated catalytic performance in metallic glasses, Adv. Mater. 30 (45) (2018), e1802764.
[28] P.F. Zhang, et al., Heterogeneously structured FeCuBP amorphous–nanocrystalline alloy with excellent dye degradation efficiency, Appl. Phys. A 127 (5) (2021) 330.
[29] H. Xu, et al., Boronization-induced ultrathin 2D nanosheets with abundant crystalline-amorphous phase boundary supported on nickel foam toward efficient water splitting, Adv. Eng. Mater. 10 (3) (2019), e1902714.
[30] X. Dong, et al., Improved hydrogen storage dynamics of as-milled $Mg_{22}(LaY)_2Ni_{10}$ alloy catalyzed by MoS_2, Appl. Surf. Sci. 484 (2019) 1198.
[31] D. Li, et al., Dense crystalline-amorphous interfacial sites for enhanced electrocatalytic oxygen evolution, Adv. Funct. Mater. 32 (7) (2021), e2107056.
[32] Z. Fakhraai, J.A. Forrest, Measuring the surface dynamics of glassy polymers, Science 319 (5863) (2008) 600.
[33] K.Q. Huang, et al., Direct observation of atomic-level nucleation and growth processes from an ultrathin metallic glass films, J. Appl. Phys. 119 (1) (2016), 014305.
[34] C.R. Cao, et al., Liquid-like behaviours of metallic glassy nanoparticles at room temperature, Nat. Commun. 10 (1) (2019) 1966.
[35] W. Yao, et al., Tailoring nanostructured Ni-Nb metallic glassy thin films by substrate temperature, Acta Mater. 194 (2020) 13.
[36] M.A. Gibson, G.W. Delamore, Nucleation and growth-kinetics of stable and metastable eutectic in FeSiB metallic glasses, Acta Metall. Mater. 38 (12) (1990) 2621.
[37] E. Illekova, et al., The complex characteristics of crystallization of the $Fe_{75}Si_{15}B_{10}$ glassy ribbon, Acta Metall. Mater. 32 (17) (1997) 4645.

[38] Z. Jia, et al., Disordered atomic packing structure of metallic glass: toward ultrafast hydroxyl radicals production rate and strong electron transfer ability in catalytic performance, Adv. Funct. Mater. 27 (38) (2017), e1702258.
[39] A. Agrawal, P.G. Tratnyek, Reduction of nitro aromatic compounds by zero-valent iron metal, Environ. Sci. Technol. 30 (1) (1996) 153.
[40] J.S. Cao, et al., Reducing degradation of azo dye by zero-valent iron in aqueous solution, Chemosphere 38 (3) (1999) 565.
[41] J.P. Saxe, et al., Enhanced biodegradation of azo dyes using an integrated elemental iron-activated sludge system: I. Evaluation of system performance, Water Environ. Res. 78 (1) (2006) 19.
[42] S. Nam, P.G. Tratnyek, Reduction of azo dyes with zero-valent iron, Water Res. 34 (6) (2000) 1837.
[43] C. Zhang, Q. Sun, Annealing-induced different decolorization performances of Fe-Mo-Si-B amorphous alloys, J. Non Cryst. Solids 470 (2017) 93.
[44] D.H. Kim, et al., Phase separation in metallic glasses, Prog. Mater. Sci. 58 (8) (2013) 1103.
[45] G. Herzer, Grain size dependence of coercivity and permeability in nanocrystalline ferromagnets, IEEE Trans. Magn. 26 (5) (1990) 1397.
[46] H.A. Murdoch, C.A. Schuh, Estimation of grain boundary segregation enthalpy and its role in stable nanocrystalline alloy design, J. Mater. Res. 28 (16) (2013) 2154.
[47] A. Khalajhedayati, T.J. Rupert, High-temperature stability and grain boundary complexion formation in a nanocrystalline Cu-Zr alloy, JOM 67 (12) (2015) 2788.
[48] A. Takeuchi, A. Inoue, Classification of bulk metallic glasses by atomic size difference, heat of mixing and period of constituent elements and its application to characterization of the main alloying element, Mater. Trans. 46 (12) (2005) 2817.
[49] P. Luo, et al., Microscopic structural evolution during ultrastable metallic glass formation, ACS Appl. Mater. Interfaces 13 (33) (2021) 40098.
[50] A. Kraut-Vass, et al., NIST X-ray Photoelectron Spectroscopy Database, Measurement Services Division of the National Institute of Standards and Technology (NIST) Technology Services, 2012.
[51] M. Descostes, et al., Use of XPS in the determination of chemical environment and oxidation state of iron and sulfur samples: Constitution of a data basis in binding energies for Fe and S reference compounds and applications to the evidence of surface species of an oxidized pyrite in a carbonate medium, Appl. Surf. Sci. 165 (4) (2000) 288.
[52] T. Yamashita, P. Hayes, Analysis of XPS spectra of Fe^{2+} and Fe^{3+} ions in oxide materials, Appl. Surf. Sci. 254 (8) (2008) 2441.
[53] M.C. Biesinger, et al., Resolving surface chemical states in XPS analysis of first row transition metals, oxides and hydroxides: Cr, Mn, Fe, Co and Ni, Appl. Surf. Sci. 257 (7) (2011) 2717.
[54] J.A. Mielczarski, et al., Role of iron surface oxidation layers in decomposition of azo-dye water pollutants in weak acidic solutions, Appl. Catal. B 56 (4) (2005) 289.
[55] M.S. Burke, et al., Cobalt-iron (oxy) hydroxide oxygen evolution electrocatalysts: The role of structure and composition on activity, stability, and mechanism, J. Am. Chem. Soc. 137 (10) (2015) 3638.
[56] Z. Jia, et al., Role of boron in enhancing electron delocalization to improve catalytic activity of Fe-based metallic glasses for persulfate-based advanced oxidation, ACS Appl. Mater. Interfaces 12 (40) (2020) 44789.
[57] H.L. Lien, W.X. Zhang, Nanoscale Pd/Fe bimetallic particles: Catalytic effects of palladium on hydrodechlorination, Appl. Catal. B 77 (1–2) (2007) 110.
[58] C.M. Su, R.W. Puls, Kinetics of trichloroethene reduction by zerovalent iron and tin: Pretreatment effect, apparent activation energy, and intermediate products, Environ. Sci. Technol. 33 (1) (1999) 163.
[59] K.M. Carroll, et al., Explaining the transition from diffusion limited to reaction limited surface assembly of molecular species through spatial variations, Langmuir 34 (1) (2018) 73.
[60] S.Q. Chen, et al., Effect of residual stress on azo dye degradation capability of Fe-based metallic glass, J. Non Cryst. Solids 473 (2017) 74.
[61] B. Xu, et al., Microdroplet-guided intercalation and deterministic delamination towards intelligent rolling origami, Nat. Commun. 10 (1) (2019) e5019.
[62] S. Xie, et al., The pivotal role of boron in improving the azo dye degradation of glassy Fe-based catalysts, ChemCatChem 12 (3) (2020) 750.